Scientific paper

Structure and Dielectric Properties of Electrochemically Grown ZrO_2 Films

Andrea Gomez Sanchez,[1] Maria Katunar,[1] Wido Schreiner,[2] Gustavo Duffó,[3,4] Silvia Ceré[1,]* and David J. Schiffrin[5]

[1] *División Corrosión - INTEMA, Universidad Nacional de Mar del Plata - CONICET, Juan B. Justo 4302, B7608FDQ Mar del Plata, Argentina.*

[2] *LSI – LANSEN, Departamento de Física, UFPR. Curitiba, Brazil.*

[3] *Departamento de Materiales, Comisión Nacional de Energía Atómica, CONICET, Av. Gral. Paz 1499, B1650KNA San Martín, Buenos Aires, Argentina.*

[4] *Universidad Nacional de Gral. San Martín, Av. Gral. Paz 1499, B1650KNA San Martín, Buenos Aires, Argentina.*

[5] *Chemistry Department, University of Liverpool, L69 7ZD, United Kingdom.*

* *Corresponding author: E-mail: smcere@fi.mdp.edu.*

Received: 16-09-2013

Paper based on a presentation at the 4th RSE-SEE 2013 Symposium on Electrochemistry in Ljubljana, Slovenia

Abstract

The dielectric properties of electrochemically grown zirconium oxide films by anodisation of zirconium in 1.0 mol dm^{-3} phosphoric acid solution were investigated in a 3 to 30 V potential range with a view to inducing surface modifications for eventual use in biomedical and electronic applications. The oxide films grown at different potentials were characterised by Atomic Force Microscopy, X-ray photoelectron and Raman spectroscopies; the latter demonstrated the incorporation of phosphate ions into the passive films. Flat band potentials calculated from the Mott-Shottky analysis of the oxides semiconducting properties confirm the bilayer structure of the films. The oxide dielectric permittivity was evaluated from impedance spectroscopy measurements and the film oxide model proposed gave values independent of the oxide growth potential.

Keywords: Zirconium, EIS, anodic films, XPS, Raman spectroscopy of anodic films

1. Introduction

The rapid increase in demand of medical implants requires materials of high chemical resistance in biological environments. For this, the mechanical properties and good biocompatibility of zirconium and some of its alloys make them highly suitable for biomedical applications.[1,2] *In vivo* studies have shown that zirconium promotes osseointegration and that its cytotoxicity is very low, even less than for titanium alloys,[3,4] mainly due to the presence of protective oxide layers. These films decrease the corrosion rate minimising metal ion release to the biological media, thus facilitating osseointegration.[5–8] For this, increased thickness of the native film as well as modification of surface morphology for improving surface porosity and roughness is required. The enhancement of barrier properties and porosity can improve bone growth in contact with the implant.[9] In addition, roughness in the nanoscale appears to promote cell proliferation.[10,11]

Anodisation in phosphate containing electrolytes is a route for surface modification that can improve osseointegration as well as corrosion resistance of the implant materials.[12,13] Thus, biocompatibility is strongly dependent on surface properties.[14,15] The anodisation process of valve metals and specifically, the incorporation of ions into the surface film structure during growth is a complex process. Since the film thickness obtained by anodisation is in the nanometer range, its characterisation can provide structural information relevant to osseointegration.[16]

Anodic growth of zirconium oxides has been extensively studied in a wide variety of media[17–24] and growth conditions.[25] Electrolyte anions are more readily incorporated in films during anodisation in acid compared with alkaline electrolytes[17,18] and this can affect film structure, growth kinetics, dielectric behaviour and surface defect density.[24,26] Importantly, altering the semiconducting properties of the oxide could be a tool for inducing particular biological responses.[27]

Since these factors determine the success of possible applications of Zr, such as permanent biomedical implants,[12,13] corrosion resistant materials for the nuclear,[28] and importantly, high *k* dielectric materials for the microelectronics industry,[29–31] the aim of this work was to study the electrochemical properties of zirconium anodic oxides grown in phosphoric acid by a combination of spectroscopic (Raman and X-Ray Photoelectron Spectroscopy, XPS), electrochemical (polarisation curves, Electrochemical Impedance Spectroscopy, EIS) and surface imaging (Atomic Force Microscopy, AFM).

2. Experimental

2. 1. Material and Anodising Treatment

Pure zirconium sheets (99.5%, Roberto Cordes S. A., Argentina, see Table SI 1) were used, from which 20 × 15 × 0.127 mm specimens were cut. A copper wire attached to one extreme of the sample by passing it through a hole on the top of the sample and twisting it back on itself served as electrical contact. The contact was insulated from the solution by coating with transformer acrylic insulating lacquer (Delta Electroquímica SRL, Argentina). Before electrochemical treatment, the samples were cleaned with acetone (Sintorgan, analytical grade), dried in air and stored in a desiccator. No chemical etching of the surface, for example, with HNO_3–HF mixtures, was employed since this can result in fluoride contamination and consequent alteration of the properties of the oxides formed.[17]

Oxide growth was carried out in a two-electrode cell using a stainless steel mesh as counter electrode.[32,33] The electrodes were anodised for 60 minutes in 1.0 mol dm^{-3} H_3PO_4 (Sigma-Aldrich analytical grade, 85.0%) at constant total applied potential between 3 and 30V; deionised water (18.2 MΩ cm, Millipore) was used throughout.

2. 2. Surface Characterisation

Surface composition was determined by X-ray photoelectron spectroscopy using a VG Microtech ESCA 3000 system. Survey and high resolution scans of the main spectral peaks were recorded. The binding energies (BE) are referenced to a binding energy for C 1s of 284.5 eV. Raman spectra of the anodic oxides was determined with an Invia Reflex confocal Raman microscope (Renishaw, UK) using a 514 nm argon laser with a 50× objective lens. No thermal effects were observed on the samples during these measurements. Two roughness parameters, R_a (roughness average) and R_{rms} (root mean square roughness), were calculated from 40 × 40 μm images obtained in contact mode with an Agilent 550 AFM microscope (Agilent Technologies, USA.) Between 6 and 10 measurements were carried out for each sample to ensure reproducibility. Image analysis was carried out with Gwyddeon free software.[34] Different area selection criteria have been previously chosen to estimate surface roughness by AFM. For example Löberg *et al.* used sampling areas from 3 × 3 to 10 × 10 μm in a detailed study of surface roughness parameters[35] whereas Samyn *et al*. employed different areas of up to 15 × 15 μm in a comparative study of non-contact profilometry and atomic force microscopy.[36] Roughness measurements provide an objective way of relating electrochemical properties of anodic oxides to unit area that is often missing in studies of valve metals, making it difficult to compare literature results.

2. 3. Electrochemical Studies

The oxide-filmed electrodes were studied in a conventional three electrode cell using a saturated calomel electrode as reference and a platinum wire as counter electrode. The electrolyte was 1.0 mol dm^{-3} H_3PO_4 and the electrode was stabilized for 40 minutes in this solution at open circuit before the measurements, which were carried out with a Reference 600™ Potentiostat-Galvanostat-ZRA (Gamry Instruments, USA). Impedance measurements to obtain the corresponding Mott–Shottky plots[37] were performed at 1000 Hz using a 10 mV rms perturbation signal. Linear sweep voltammetry was measured at a sweep rate of 5 mV s^{-1}.

Electrochemical impedance spectroscopy (EIS) data were obtained with a PCI4 750/potentiostat/galvanostat/ZRA™ (Gamry Instruments, USA). The amplitude of the perturbation signal was 10 mV rms around the corrosion potential (E_{corr}) and the impedance was measured between 10^{-2} and 10^6 Hz. The data were fitted to equivalent circuit models with Zplot for Windows software.[38] All potentials were referred to a saturated calomel electrode (SCE, Radiometer Analytical, France).

3. Results and Discussion

3. 1. Raman Spectroscopy

Fig. 1 compares the Raman spectra for a zirconium anodic oxide grown at 30 V with untreated Zr at different points in a line at the surface, showing a uniform spectroscopic response; the absence of domains indicates uniform surface composition.

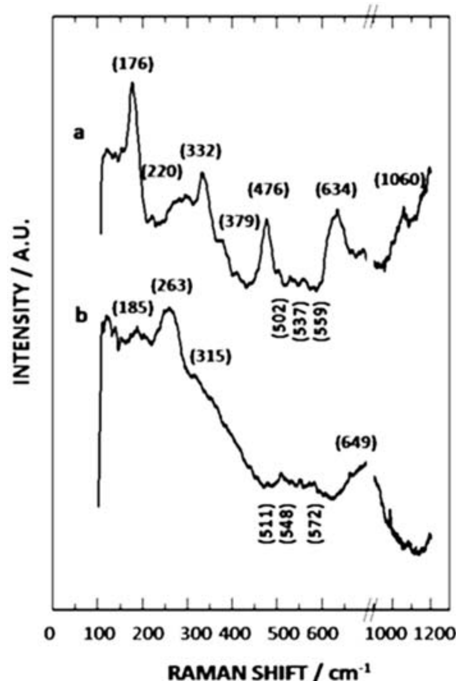

Figure 1. Raman spectra obtained for (a) the zirconium anodic oxide grown at 30 V in 1.0 mol dm^{-3} phosphoric acid and (b) for the as-received zirconium sample.

Table 1 compares these results with those for amorphous, monoclinic and tetragonal zirconia. All the peaks can be reasonably well assigned to monoclinic ZrO_2 for the anodised samples and to tetragonal ZrO_2 for the as-received samples, despite a shift of approximately 2 cm^{-1} observed compared with ZrO_2 powder.[39–41] Peaks belonging to tetragonal zirconia were not present in the anodised zirconium in agreement with XRD data that indicated mainly the presence of monoclinic zirconium oxide for films grown both thermally and electrochemically.[28] Thus, Raman spectroscopy provides identification of the crystallographic phases present in these very thin anodic oxide films. A small proportion of the tetragonal phase could only be detected by selective area diffraction. The formation of the tetragonal/cubic phase has been observed for zirconia deposited from the gas phase by radio frequency (RF) sputtering from a pure ZrO_2 target in an Ar plasma.[42] By contrast, only the monoclinic structure was obtained when ZrO_2 was obtained by reactive sputtering in the presence of oxygen. Although these preparation methods are very different, electrochemical oxidation produce films similar to those prepared in vacuum by reactive sputtering under oxidising conditions.[42]

Raman spectra showed also an additional band in the high wavenumber region, at 1060 cm^{-1}, which was absent in the as-received Zr, indicating the incorporation of phosphates from the anodising solution.[24,26] Moreover, anion incorporation is greater during the initial stages of oxide formation when the current density is high.[17,18,43] From Raman spectra measurements, this band has been assigned to zirconium pyrophosphate incorporated within monoclinic zirconia obtained by pyrolysis of ZrO_2 in the presence of $(NH_4)_2HPO_4$.[44]

Table 1. Comparison of Raman spectral peaks observed for Zr as received and anodised at 30 V with literature data for ZrO_2 35–37 vs: very sharp, s: sharp, w: weak, b: broad

Anodic oxide grown at 30 V (cm^{-1})	As received Zr (cm^{-1})	Monoclinic ZrO_2 (cm^{-1})	Tetragonal ZrO_2 (cm^{-1})	Amorphous ZrO_2 (cm^{-1})
152		158	148m	
176		174vs		
		185	186vs	180–190s
221		219m		220wb
	263		255–265s	
		305m		
	315		310–320m	
332		334s		
		347m		
376		380s		
476		476vs	475m	
502	511	505m		500–570wb
532		537m		
	548			
559		559m		
	572			
		616s		
634		638s		
	649		625–640s	

3. 2. XPS Analysis

XPS measurements of anodised samples showed a characteristic P 2p peak.[45] Gaussian fitting gave binding energies (BEs) of 133.4 and 133.3eV for oxides grown at 12 and 24 V, respectively (Figure 2a). Therefore, the nature of the phosphorous species incorporated is independent of the growth potential and clearly indicates the presence of P-O functional groups,[46,47] confirming the Raman spectra results.

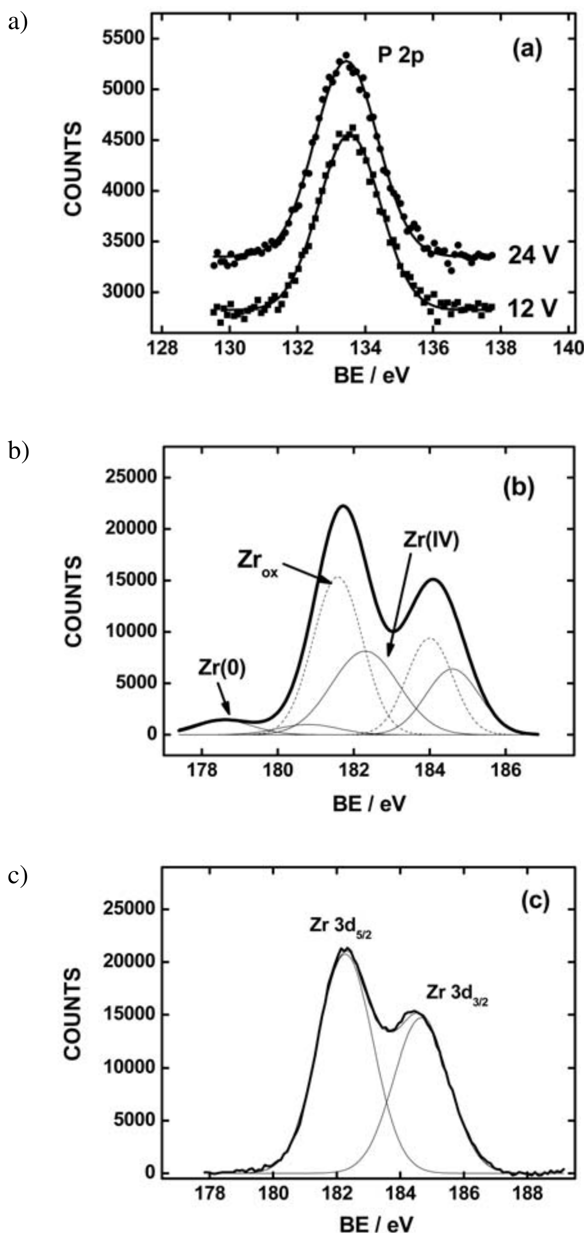

Figure 2. XPS detailed scans for (a) the P 2p region for samples anodised at 12 and 24 V; (b) Zr 3d region for the as-received material and (c) the same after anodisation at 24 V. The XPS data has been deconvoluted using Gaussian functions. Lower oxidation states are present in the as received sample.

Figures 2b and 2c show detailed spectra of the zirconium 3d region for the as-received material and for a sample with oxide grown at 12 V. A surface atomic ratio for Zr to P of 4.5 is obtained from the integrated P 2p and Zr 3d peaks and the corresponding atomic sensitivities[48] clearly demonstrating the replacement of oxygen by phosphate containing species, in agreement with the Raman results.

Spectral deconvolution of the Zr $3d_{5/2}$ and $3d_{3/2}$ bands for the anodised Zr (Fig 2c) gave binding energies of 182.3 and 184.7 eV, respectively. The spin-orbit splitting observed was 2.4 eV, as previously observed[45,47]. The $3d_{5/2}$ BE measured was similar to the literature recommended value for Zr^{4+} in ZrO_2, of 182.2 eV[42,49] for samples prepared by reactive sputtering of a zirconia target in the presence of oxygen. Fig. 2b shows a spectral deconvolution of the as-received sample. In this case, the main XPS peak has a BE lower than that of the anodised samples, with a BE for the $3d_{5/2}$ peak at 181.7 eV, lower than the value for ZrO_2. In order to get as much as possible an unbiased result, the 3d 3/2 and 3d 5/2 binding energies were fixed to the well known values for Zr(0) and Zr(IV)[49] and then the non-linear regression program was allowed to choose the best values corresponding to the other oxide species present, without attempting to separate these additional contributions. The main signals were found at binding energies of 181.6 and 184.0 eV, most likely related to the 3d level of Zr(III) suboxide.[49,50]

Due to the difficulties in deconvoluting reliably a multi-peak spectrum, this peak has been simply labelled as ZrO_{ox}, corresponding to lower oxidation states of zirconium present at the Zr-oxide interface.[49–52] The minor feature at 178.5 eV (Figure 2b) corresponds to the Zr^0 substrate (BE for Zr^0 $3d_{5/2}$ = 178.79 eV[44]). As would be expected, all these suboxide features could not be observed for the fully oxidised samples investigated. The results in Fig. 2b indicate that the oxidation state of Zr in the oxide in direct contact with the metal is lower than (IV). Gradients of oxidation state have been known for a long time for passive Fe oxides[30] and are important in determining the overall electrical response of the film.

3. 3. Surface Roughness

Surface roughness affects the interpretation of impedance measurements in at least two ways. An increase in area of the oxide-solution interface increases the volume of the polarisable dielectric oxide and hence, gives lower values of the impedance (higher film capacitance contributions). In addition, the different electric field pathways caused by film roughness give rise to a frequency dispersion characteristic of a transmission line. This can be modelled using a constant phase element component (see Section 3.6).[53,54] These effects become important when the average surface roughness length is comparable to the thickness of the oxide film.

Surface roughness parameters used for the characterisation of the osseointegration properties of dental implants have been extensively discussed by Löberg et al.[35] but only two parameters, R_a and R_q, have been calculated from AFM measurements in the present work since these can be more readily related to engineering considerations and also provide surface structural information.[55–57] *R*a is the arithmetic average of the absolute values of the surface heights referred to the mean:[56]

$$R_a = \frac{1}{n}\sum_{i=1}^{n}|y_i - y_{av}|$$

n = number of positions sampled, y_i = film height at position i and y_{av} = average film height. The parameter R_q is the root mean square of the surface topography given by:

$$R_q = \sqrt{\frac{1}{n}\sum_{i=1}^{n}|y_i - y_{av}|^2}$$

The dependence of R_a and R_q on growth potential is shown in Fig. 3a. The difference between R_a and R_q is the standard deviation (SD) from the mean. The initial roughness of the material had a SD of approximately 25% that increased slightly to 27% for a surface anodised at 30 V. The similarity of the percentual differences in the values of R_a and R_q indicates that the standard deviation from the mean does not change significantly with oxide thickness, i.e., percentual deviations from the average height are not very large. R_q and R_a are often linearly related to each other through the surface geometry[56] and the dependence of R_q on R_a is shown in Fig. 3b. The slope was 1.25, a value commonly encountered for surfaces having a random Gaussian distribution of surface heights.[55–57]

The above observations indicate that the overall surface profile does not alter significantly with increasing oxide thickness although the differences between valleys and troughs in the film increase with thickness. A correction to the effective surface area for the calculation of parameters such as carrier number density derived from the Mott-Shottky plots, current density and for the impedance analysis is required. For this, the surface area factor, S_{AR}, defined as the ratio of real to nominal area obtained from the AFM measurements was employed. Only short range surface features of dimensions in the nanometre range, which represent the largest contribution to the value of S_{AR}, were considered. S_{AR} increases with anodising potential (Fig. 4) indicating small changes in the interfacial topography, in agreement with previous reports for Zr and Zircaloy-2 in various electrolytic media.[58] The values of S_{AR} were used to refer the electrochemical results to unit area of the oxide-solution interface.

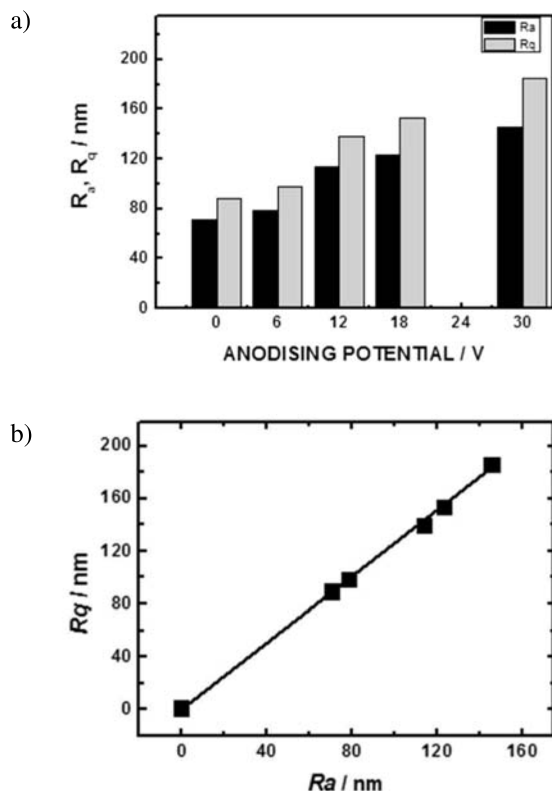

Figure 3. (a) dependence of the Ra and Rrms roughness parameters on anodisation potential for the zirconium samples studied. (b) Dependence of Rrms on Ra.

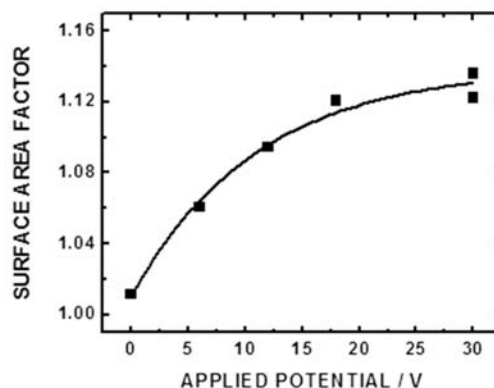

Figure 4. Dependence of the surface area factor on anodisation potential for the zirconium samples studied.

3. 4. Semiconducting Properties of the Anodic Films

Changes in electronic properties of the anodic oxide films on zirconium due to electrolyte ion incorporation are still a matter of controversy. For instance, ZrO_2 films change from a pure dielectric to an *n*-type semiconductor in contact with 0.5 mol dm^{-3} H_2SO_4[59] whereas anodic zirconium oxides grown in lactic acid behave as purely dielectric materials.[60] A transition from semiconducting to insulating behaviour has been reported when anodising Zr in NaOH.[61]

The semiconducting properties of the ZrO_2 films were investigated using Mott–Shottky plots.[62a] The capacitance of the films grown at different potentials was measured at potentials well below the film growth potential to ensure that no additional growth occurred during these measurements. For a semiconductor in contact with an electrolyte solution, the dependence of the space charge capacitance on potential under depletion conditions is given by:[53]

$$\frac{1}{C_{sc}^{\ 2}} = \frac{2}{qN_d\varepsilon_r\varepsilon_0}\left(V - V_{fb} - \frac{kT}{q}\right). \quad (1)$$

where C_{sc} is the capacitance of the space charge region, q is the charge of the carriers, N_d is the carrier number density (cm^{-3}), ε_r is the relative dielectric permittivity of the film, ε_0 is the permittivity of free space (8.85×10^{-14} F cm^{-1}), V is the applied potential, V_{fb} is the flat band potential, k is the Boltzman constant and T the absolute temperature. The sign of q indicates the type of semiconductor film present (*n*- or *p*-); the number density of charge carriers can be calculated from the slope and the intercept gives the flat band potential.[36]

Some typical results obtained are presented in Figure 5, where the linearity expected from Eq. 1 is observed, also confirming *n* type behaviour. The apparent flat band potential (V_{fb}) for different growth potentials corresponding to $C^{-2} = 0$ was, however, very negative with V'_{fb} = (–11±4) V, an unrealistic value for the band structure of the oxide investigated. Very large absolute values for (V'_{fb}) have also been previously observed for oxide fi-lms.[62a] De Gryse *et al.* demonstrated that if the oxide film comprises not only a depletion layer but also an insulating dielectric in series, the classical Mott–Shottky equation becomes:[63]

$$\frac{1}{C^2} = \frac{1}{C_{ox}^2} + \frac{2}{qN_d\varepsilon_r\varepsilon_0}\left(V - V_{fb} - \frac{kT}{q}\right) \quad (2)$$

where C in the measured capacitance and C_{ox} is the capacitance of the insulating oxide dielectric *in series* with the space charge capacitance.[27,53,62a–64] The Helmholtz layer capacitance is not considered here since its value for the oxide-solution interface is very high, of the order of 100 $\mu F\ cm^{-2}$.[27] This value is much greater than that of the ZrO_2 filmed electrodes and therefore, its impedance can be neglected compared with that of the film.

The dual layer structure is the main difference between an anodic Zr oxide film and a classical semiconductor and a general analysis of this question has been discussed by Albery et al.[65] Thus, although the slopes of the C^{-2} vs V plots are linear and can be used to calculate correct values of N_d,[27,66] the flat band potential cannot be obtained from them since the series capacitance term includes an additional contribution to the values of C^{-2}. This is the reason for the observation of very negative apparent values of V_{fb} when using Equation (1).

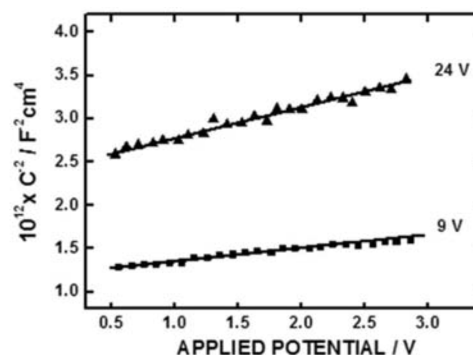

Figure 5. Mott-Schottky plots of zirconium anodised at 9 (■) and 24 V (▲) in 1.0 mol dm^{-3} phosphoric acid.

The anodic oxide films on Zr and its alloys have a bilayer structure consisting of a thin inner layer where conduction occurs through oxygen vacancies and/or zirconium interstitials, and of a slightly porous and more defective outer dielectric layer.[28,41,66–68] The latter can be permeated by the contacting solution thus complicating the impedance analysis by introducing frequency dispersion effects. This bilayer structure is common to many passive films and the analysis developed by Macdonald et al.[67,69,70] for Zr and its alloys has been successfully applied to other valve metals.

The calculation of the carrier number density requires a value of the relative dielectric permittivity (ε_r) of the oxide film. The electrical properties of Zr has been the subject of many studies due to the use of Zr in the nuclear industry and more recently, ZrO_2 have received a great deal of attention since its very wide band gap and high dielectric permittivity makes it an attractive gate material in electronics. The properties of the oxides studied for these two applications present, however, significant differences. For the former, the materials studied have been obtained by anodic oxide growth or oxidation in aqueous solutions whereas for the latter, gas phase preparation methods have been exclusively employed, e.g., Atomic Layer Deposition or Chemical Vapour Deposition.

The variety of dielectric permittivity results reported in the literature is due to the different phases formed and their stability ranges. For example, ε_r for the monoclinic, cubic and tetragonal crystal structures have been estimated as 19.7, 36.8 and 46.6, respectively.[71] The stability ranges of these structures is <1400, 1400–2570 and 2570–2980 K, respectively[72] and therefore, materials prepared at room temperature would be expected to display preferentially the monoclinic structure.

A summary of values of ε_r obtained under conditions similar to those employed in the present work is shown in Table 2. Most of the values reported are within the range of 20 to 30. For the purpose of the following analysis, a value of 30 has been used.[62a] In contrast with semiconductors-metal junctions, the donor density is strongly dependent on anodising potential (Figure 6). The

Table 2. Collection of relevant dielectric permittivity values for ZrO_2

Reference No	ε_r (Dielectric Permittivity)	Comments
23	25–29	Anodising at a constant current density in 0.1 mol dm^{-3} ammonium pentaborate electrolyte
18	21.4	Oxides obtained by anodisation in sodium hydroxide; ammonium borate and sodium sulphate up to the breakdown potential
20	21	
60	21	
62a	29.9	Anodic film grown in phosphoric acid.
77	25–27	Combined neutron diffraction reflectrometry and electrochemical measurements
78	20	Anodisation in various electrolytic media and applied potentials (up to 420 V).

N_d values reported by A. Goosens et al.[62a] were higher than those obtained in the present work, which might result from differences in the frequency range employed and from assumptions on the surface area factor of the samples. The N_d results obtained in the present work are in good agreement with those reported by Sato for different refractory metals[43] and for zirconium anodic oxides.[59] The decrease in N_d observed for higher oxide growth potentials is also in agreement with observations for other valve metals[73–75] and for zirconium-niobium alloys.[76] This behaviour can be ascribed to a decrease in the density of oxide defects with increasing film thickness.

The oxide growth current density decreased rapidly to very low values during the first minute of anodisation, when the main increment of the oxide film thickness actually occurs. During the remaining film growth period, the applied potential leads to a decrease in lattice defects and thus to an additional reduction of the carrier density due to film ageing.

The simple model of two ideal capacitors in series described above, although it provides a reasonable structure for analysing the semiconducting properties of the anodic film, is, however, inappropriate to describe fully the electrical properties of the oxide films and a more complex interfacial model is required.[67–69] It is possible, in principle, to obtain additional information from equation (2) such as the value of the series capacitance C_{ox} by making use of the estimate of the flat band potential of ZrO_2 by Kung et al.[62b] Correcting for differences in reference electrodes and pH, V_{fb} = 1.30 V vs SCE at pH = 1.08, corresponding to 1mol dm^{-3} H_3PO_4 The estimate of C_{ox} from these data is too uncertain due to the large extrapolation required. This quantity was determined form ac impedance measurements (see below).

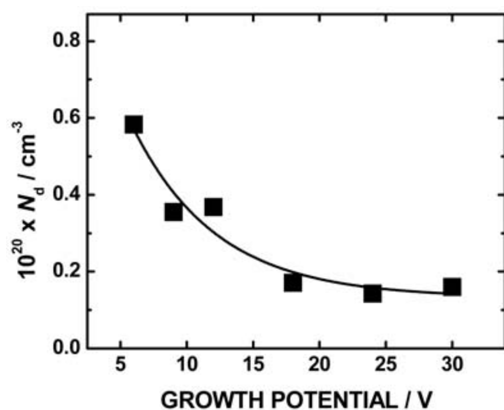

Figure 6. Dependence of the charge carrier number density on anodising potential determined from the Mott-Shottky analysis.

There is, however, an additional problem for establishing the contribution of the space charge capacitance in the analysis of bilayer oxide structures such as this since this requires the knowledge of the actual potential drop across the depletion region. This is not given by the actual applied potential referred to V_{fb} due to the presence of an insulating oxide in series with the semiconducting layer in contact with the metal. In order to make a quantitative assessment, the applied potential has to be corrected by the ratio C_{SC}/C_{ox}. Previous work indicated that the space charge region contribution to the total impedance is not very large as a consequence of the small actual potential drop across the space charge region.[27] Since the value of C_{ox} cannot be reliably obtained from the Mott-Schottky plots and considering the other uncertainties mentioned above, we have preferred to treat the inner layer as an additional constant phase element in the equivalent circuit (see below, discussion of Fig. 9) 3.5. Electrochemical behaviour

Anodic film oxide growth is shown in Fig. 7 when consecutive potential sweeps are applied up to increasingly anodic switching potentials. The first scan (curve (a)) shows a large current plateau associated with a high field oxide growth mechanism (Ref. 79 and references cited therein). The return sweep still shows some growth as the current decays to very low values. Importantly, further film growth in the following sweep does not appear until the potential is more positive than the previous switching potential (curve (b)), indicating that no significant film dissolution takes place, as expected for the extremely insoluble zirconium oxide formed. The third cycle (curve (c)) shows a similar behaviour, i.e., further growth can only take place when the field across the oxide exceeds that present at the switching potential of the previous scan. These observations are characteristic of an insoluble film following a constant field film growth mechanism. Impor-

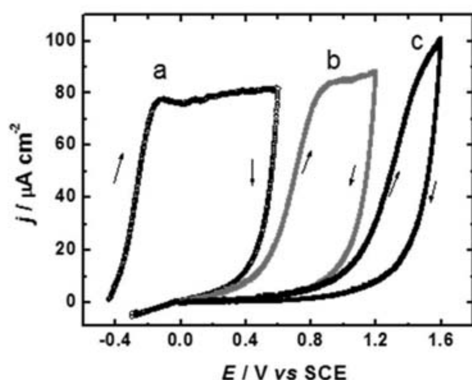

Figure 7. Anodic polarization curves for the as-received zirconium in 1.0 mol dm^{-3} H_3PO_4 at increasingly anodic switching potentials from (a) to (c). Sweep rate = 5 mV s^{-1}.

tantly, the electric field controlling film growth is present only across the oxide layer, which increases its thickness linearly with the applied field, with a dependence given by $\delta_v = \mathrm{d}d/\mathrm{d}V = (2.8 \pm 0.2)$ nm V^{-1} (δ_v = anodisation constant, d = film thickness, V = applied growth potential).[59,60,62a,80]

3. 6. Dielectric Film Properties

The dielectric properties of the anodic films were investigated by EIS and typical results for the anodised Zr electrodes are shown in Figure 8. For all the anodised electrodes and conditions investigated, $\frac{\mathrm{dlog}(|Z|}{\mathrm{dlog}\,(f)} < 1$ and not equal to 1, as would be the case for a dielectric without losses. This non-ideal capacitive behaviour,[53,54] is usually observed for oxide films grown on valve metals.[81–84] In addition, a shift of the phase angle with anodising potential is observed at high frequencies, a consequence of the increase in oxide thickness.[85] that also leads to a similar increase of the total impedance modulus extrapolated to zero frequency indicating the formation of more resistive films.

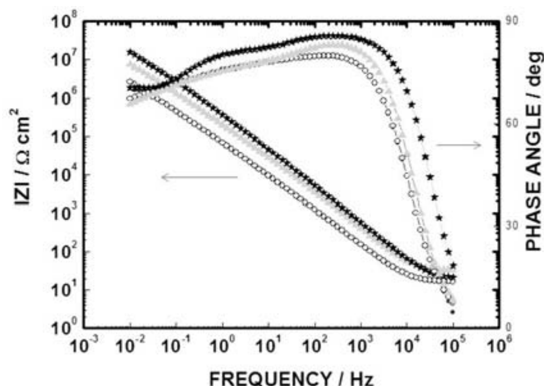

Figure 8. Bode plots of the as-received and anodised zirconium at different potentials in 1.0 mol dm^{-3} phosphoric acid: Anodising potentials: 9V (0), 24 V (▲) and 30 V (*).

To account for these observations, the oxide film was modelled as a bilayer structure involving an inner compact layer in contact with a partially porous outer layer that can include electrolyte from the solution (Figure 9a).[67,69,70] The equivalent circuit corresponding to this structure is given in Figure 9b. This model attempts to capture the main properties of the oxide film for all the growth potentials whilst keeping a minimum number of variables to reflect a realistic physical model.[67,77,86–89] This corresponds to an idealised model, ignoring contributions due to ionisable surface states, films homogeneities and the presence of the native oxide in the interface localized at the end of the pores. Constant phase element impedance contributions (Z_{CPE}) were included[33,78,80,91] to account for deviations from a slope of –1 in the modulus Bode plot.

The oxide is considered in series with a solution resistance R_e. The equivalent circuit employed recognises the distinction between the barrier-like inner layer and the porous outer layer discussed before. CPE_1 is a constant phase element corresponding to the total oxide capacitance, from the solution to the metal, involving a dielectric with a range of relaxation times. [33,78,80,91] R_1 relates to the resistance of the electrolyte present in the outer porous oxide layer and the constant phase element CPE_2 describes the inner layer of the oxide film, between the bottom

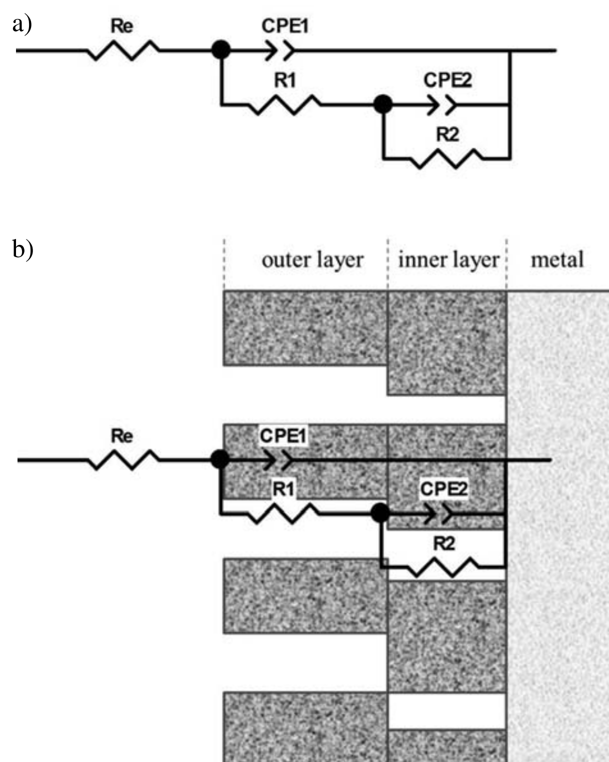

Figure 9: (a) Equivalent circuits employed for data fitting, (b) equivalent circuit corresponding to a bilayer structure involving an inner compact layer in contact with a partially porous outer layer that can include electrolyte from the solution.

of the pores and the metal substrate. R_2 has the same physical meaning as R_1 but involving only the inner oxide layer in direct contact with the metal. In common with many EIS analyses, other equivalent circuits can be proposed to fit the impedance spectrum but the model chosen reflects the proposed structure of oxides grown on valve metals. The suitability of the model can be judged, as described below, from the values of the parameters obtained.

The impedance of a constant phase elements, Z_{CPE}, is given by:[92]

$$Z_{CPE} = 1/Q(j\omega)^{\alpha} \tag{3}$$

where Q is a parameter independent of frequency and α is a coefficient associated with system homogeneity. When $\alpha = 1$, Q represents the ideal capacitance of the system. When $\alpha<1$, the system shows a behaviour that can be attributed to surface heterogeneities such as grain boundaries, steps or different crystal faces on polycrystalline materials, or to a distribution of time constants within the oxide.[54,77,92–95]

The impedance data shown in Fig. 8 were fitted to the circuit shown in Figure 9b.[93,94] The solid lines show the fitted data at each anodising potential and Table 3 shows the main parameters obtained corresponding to the model shown in Fig. 9b. The values of α_1 show little spread ($\alpha_1 = 0.94 \pm 0.02$) and are close to unity, indicating a ZrO_2 film behaviour close to that of an ideal capacitor. The model did not allow distinguishing between R_1 and R_2 for the results at 0 and 3 V and only a value of $R_1 + R_2$ could be extracted from these data. The values of R_1 were in all other cases much smaller than those of R_2, as would be expected for a film with an outer porous layer (see Fig. 9a–b). Thus, the total film resistance is very close to the value of R_2.

R_2 is equivalent to the total resistance of the electrolyte present in the pores in contact with the metal surface. The resistance of a single pore (R_p) is given by:

$$R_p = \frac{l_p}{\kappa A_p} \tag{4}$$

where l_p is the pore length, κ is the specific conductance of 1 mol dm^{-3} H_3PO_4 at 25 °C (0.058 S cm^{-1} [96]) and A_p is the projected area of the pore. From the measured value of R_e (Table 3), for a maximum pore depth of 84 nm and ignoring tortuosity factors, the average value of the total apparent pore area was $(1.5 \pm 0.7) \times 10^{-12}$ cm^2, i.e., the film porosity has a very small value and therefore the dielectric properties that can be calculated refer to an oxide with a negligible contribution to the permittivity due to film porosity.

The relationship between the capacitance of a parallel plate capacitor and dielectric permittivity is given by:[54]

$$C = \frac{\varepsilon_{eff}\varepsilon_0 A}{d} \tag{5}$$

where ε_0 is the permittivity of free space ε_{eff} is the average dielectric permittivity of the oxide film and d the plate separation. In order to establish a relationship between a non-ideal capacitor and dielectric permittivity, a model taking relaxation time constants must be considered. For this, an effective film capacitance (C_{eff}) has to be related to film models.[92–94] Two approaches can be used to define an effective film capacitance from the circuit model parameters (Figure 9). The method described by Brug et al.[93] gives:

$$C_{eff} = Q_1^{1/\alpha}(R_e^{-1} + R_t^{-1})^{(\alpha-1)/\alpha} \tag{6}$$

where R_e is the electrolyte ohmic resistance and R_t is the total resistance of the electrolyte within the pores (R_1+R_2). Q_1 and α have the same meaning as in Equation (3), corresponding to the CPE1 element. An alternative method considers a series combination of local impedances.[54] In this case, Hsu and Mansfeld[94] proposed that C_{eff} is given by:

$$C_{eff} = Q_1^{1/\alpha} R_f^{(1-\alpha)/\alpha} \tag{7}$$

R_f is the series combination of all the resistances (R_e+R_1+R_2); all other parameters have the same meaning as in Equation (3).[95]

The dielectric permittivity was calculated from equations (5), (6) and (7) using film thicknesses calculated using the value of the anodisation constant given abo-

Table 3. Equivalent circuit parameters obtained from the non-linear regression fitting of the EIS results to the circuit in Fig. 8 and dielectric permittivity calculations.

E/ V	α_1	Q_1/ s$^{\alpha}$ Ω^{-1} / cm^{-2}	R_1 / ΩW cm^2	C_{eff} / F cm^{-2}	dδ_v /nm	ε_r
3	0.94	$(5.4 \pm 0.9) \times 10^{-6}$	$(3.4\ 1 \pm 1) \times 10^{6}$	$(2.96 \pm 0.17) \times 10^{-6}$	8.4	28.5 ± 1.4
6	0.90	$(4.4 \pm 0.1) \times 10^{-6}$	$(6.8 \pm 2) \times 10^{4}$	$(1.6 \pm 0.4) \times 10^{-6}$	16.8	30.1 ± 7.7
9	0.91	$(2.5 \pm 0.1) \times 10^{-6}$	$(3.4 \pm 1) \times 10^{4}$	$(8.9 \pm 0.8) \times 10^{-7}$	25.2	25.6 ± 2.1
12	0.93	$(1.47 \pm 0.08) \times 10^{-6}$	$(3.\ 6 \pm 1.8) \times 10^{4}$	$(7.4 \pm 0.03) \times 10^{-7}$	33.6	27.9 ± 0.1
18	0.95	$(7.3 \pm 0.2) \times 10^{-7}$	$(8 \pm 4) \times 10^{4}$	$(4.2 \pm 0.2) \times 10^{-7}$	50.4	24.2 ± 1
24	0.95	$(5.5 \pm 0.4) \times 10^{-7}$	$(4.2\ 10^{4} \pm 0.\ 3) \times 10^{4}$	$(3.4 \pm 0.1) \times 10^{-7}$	67.2	26.1 ± 0.8
30	0.97	$(3.9 \pm 0.1) \times 10^{-7}$	$(4.\ 4 \pm 0.1) \times 10^{4}$	$(3.2 \pm 0.3) \times 10^{-7}$	84.0	26.8 ± 1.7

d was calculated using δ_v = 2.8 nm V^{-1}. R_e= 28 ± 18 Ω cm^2 ε_r = 27 ± 3 (average from all potentials)

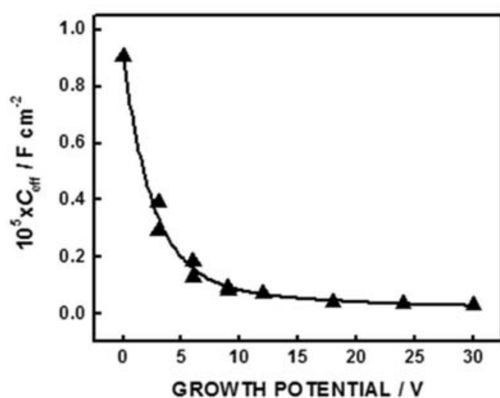

Figure 10: Dependence of C_{eff} on film growth potential. Data from different experiments are included in the Figure

ve. The dependence of C_{eff} on film growth potential is shown in Fig. 10. As expected, C_{eff} decreases with increasing growth potential due to the increase in the insulating film thickness. As discussed above, the space charge capacitance makes no significant contribution to the overall film impedance and hence, the estimated parameters provide an accurate representation of the insulating oxide film properties. The dielectric permittivity of the oxide was, therefore, estimated from C_{eff} according to equation (9).

The average value of ε_{eff} was 27 ± 3, which compares well with other estimates using different approaches, as described in Table 3. Thus, the calculation of the effective capacitance (Eqn. (8)) provides an appropriate description of the dielectric properties of the film. A similar analysis as above using a series equivalent circuit as described by Hsu and Mansfeld[54,94] gave an unrealistic high value of ε_{eff} with a very high standard deviation, of 58 ± 27 indicating that this approximation does not lead to reliable values of dielectric permittivity.

It is concluded that regardless of the complexity of the film structure, the proposed model and corresponding equivalent circuit applied to the EIS results can be conveniently employed to estimate the dielectric permittivity of an electrochemically grown oxide film of ZrO_2.

4. Conclusions

This work has attempted to characterise oxide films formed on the surface of anodised zirconium, an attractive material for biomedical and electronic applications. The inclusion of phosphorous as a zirconium phosphate in oxides grown in phosphoric acid has been demonstrated by both Raman spectroscopy and XPS. The incorporation of this anion is considered beneficial in providing good anchorage for implants and the techniques presented can serve as a control of quality of the required surface treatment for medical implants. In addition, the surface characterisation techniques employed demonstrate that the oxide formed, monoclinic ZrO_2, is stable and fast passivation kinetics indicates that no dissolution takes place. The AFM results indicate that although the amplitude of the surface features increases with anodising potential, the overall surface geometry does not alter significantly as demonstrated by the dependence of R_a on R_{ms}. Thus, simple surface roughness parameters can serve to establish the surface quality and the influence of the substrate on the structure of the oxide formed. This is an important observation that links basic measurements as described in this paper with well-established surface roughness methods employed in the characterisation of engineered components.

The electrical properties of oxide films in medical implants is an important property for establishing the level of defects in the oxide films formed. It is demonstrated that the flat band potential does not provide a simple interpretation for the band structure of the oxide but importantly, the slopes of the Mott- Shottky plots give a quantitative estimate of the carrier number density. The decrease in this quantity when increasing the applied growth potential is in agreement with the behaviour found for anodic oxide films of other pure valve metals and can be related to the changes in film defects when increasing film thickness. The rapid increase in thickness of the passive film and the absence of any significant dissolution in the passive state when increasing the anodising potential corroborates the excellent corrosion barrier properties of this material. Importantly, *the incorporation of phosphate in the film does not lead to an impairment of its barrier properties*. The impedance results demonstrate the increase in thickness of the anodic film with anodising potential and changes in thickness can be followed from impedance analysis. These results correlate with the XPS data in demonstrating clearly that without an oxidative treatment, the presence of low oxidation states of Zr on the surface or indeed, of some free metal, is observed. Thus, the electrochemical oxidation and the surface controls investigated can provide a simple route for improving the long-term stability of the anodically grown oxides.

5. Acknowledgements

Support from Consejo Nacional de Investigaciones Científicas y Técnicas, Agencia Nacional de Promoción Científica y Tecnológica and Universidad Nacional de Mar del Plata, Argentina, and from the PROSUL project, Brazil, are gratefully acknowledged. The authors also acknowledge useful discussions and comments on the analysis of surface roughness by Dr Daniel Sosa, INTEMA, Argentina.

6. References

1. K. M. Sherepo and I. A. Redžko, *Biomed*. Eng. **2008**, *38*, 77–79.

2. D. Zander and U. Köster, *Mat. Sci. Eng. A.* **2004**, *375–377*, 53–59.
3. R. Cabrini, M. B. Guglielmotti and J. C. Almagro*, Implant Dent*. **1993**, *2*, 264–267.
4. T. Hanawa, *Mat. Sci. Eng. C***. 2004**, *24*, 745–752.
5. Y. Okazaki and E. Gotoh, *Biomaterials.* **2005**, *26*, 11–21.
6. S. Hiromoto and T. Hanawa, *Electrochim. Acta.* **2002**, *47*, 1343–1349.
7. T. Hanawa, *Mat. Sci. Eng. A*.**1999***, 267*, 260–266.
8. D. H. Kohn, *Curr. Opin. Solid St. M*.**1998**, *3*, 309–316.
9. G. Mendonça, D. B. S. Mendonça, F. J. L. Aragão, and L. F. Cooper, *Biomaterials.* **2008**, *29*, 3822–3835.
10. J. C. Hansen, J. Y. Lim, L-Ch Xu, C. A. Siedlecki, D. T. Mauger and H. J. Donahue, *J. Biomech.* **2007**, *40*, 2865–2871.
11. J. Y. Lim, L-Ch. Xu, A. D. Dreiss, Z. Zhou, J. C. Hansen, C. A. Siedlecki, R. W. Hengstebeck, J. Cheng, N. Winograd and H. J. Donahue, *Biomaterials.* **2007**, *28*, 1787–1797.
12. E. Krasicka-Cydzik, *Corros. Sci*. **2004***, 46*, 2487–2502.
13. C. E. B. Marino, P. A. P. Nascente, S. R. Biaggio, R. C. Rocha-Filho and N. Bocchi, *Thin Solid Films***. 2004**, *468*, 109–112.
14. Y.-T. Sul, C.B. Johansson, Y. Jeong and T. Albrektsson, *Med. Eng. Phys*. **2001***, 23*, 329–346.
15. K. Anselme and M. Vigerelle, *J. Mater. Sci-Mater. Med*. **2006***, 17*, 471.
16. J. Lausmaa, B. Kasemo, H. Mattson and H. Odelius, *Appl. Surf. Sci.* **1990**, *45*, 189–200.
17. J. S. L. Leach and B. R. Pearson, *Electrochim. Acta.* **1984**, *29,* 1263–1270.
18. J. S. L. Leach and B. R. Pearson, *Electrochim. Acta***. 1984**, *29*, 1271–1282.
19. J. S. L Leach and C. N. Panagopoulos, *Electrochim. Acta*. **1985**, *30*, 1621–1625.
20. J. S. L Leach and C. N. Panagopoulos, *Electrochim. Acta*. **1986**, *31*, 1577–1578.
21. J. S. L Leach and C. N. Panagopoulos, *Electrochim. Acta*. **1987,** *32*, 411–414.
22. N. Khalil and J. S. L. Leach, *Electrochim. Acta.* **1986**, *31*, 1279–1285.
23. H. Habazaki, K. Shimizu, S. Nagata, K. Asami, K. Takayama, Y. Oda, P. Skeldon and G. E. Thompson. *Thin solids films.* **2005**, *479*, 144–151.
24. N. Khalil and J. S. L. Leach, *Electrochim. Acta.* **1994**, *40*, 1769–1772.
25. A. S. Mogoda, F. El-Taib Heakal and A. A. Ghoneim, *Thin Solid films.* **1992,** *219*, 146–152.
26. F. Di Quarto, S. Piazza, C. Sunseri, M. Yang and S.-M. Cai, *Electrochim. Acta.* **1996**, *41,* 2511–1522.
27. I. Petersson, J. Löberg, A. Fredriksson and E. Ahlberg, *Biomaterials.* **2009**, *30*, 4471–4479.
28. M. Oskarsson, E. Ahlberg and K. Petersson*, J. Nucl. Mater*. **2001**, *295*, 97–108.
29. J. P. Chang, Y.-S. Lin and K. Chu, *J. Vac. Sci. Technol***.** B. **2001**.*19*, 1782–1784.
30. K. J. Vetter, *J. Electrochem. Soc.,***1963.** *110,* 597–605.
31. A. Javey, H. Kim, M. Brink, Q. Wang, A. Ural, J. Guo, P. McIntyre, P. McEuen, M. Lundstrom and H. Dai, *Nature Materials.* **2002**. *1,* 241–244.
32. T. D. Burleigh and A. T. Smith*, J. Electrochem. Soc*. **1991**, *138*, 34–35.
33. J. A. Bardwell and M. C. H. Mc. Kubre, *Electrochim. Acta.* **1991**, *36*, 647–653.
34. Gwyddeon free SPM data analysis software http://gwyddion.net/.
35. J. Löberg, I. Mattisson, S. Hansson and E. Ahlberg, *Open Biomater. J*. **2010**, *2,* 18–2
36. P. Samyn, J. Van Erps, H. Thienpont and G. Schoukens, *Appl. Surface Sci*. **2011**, *257*, 5613–5625.
37. A. W. Bott, *Current Separations.* **1998,** *17*, 87–91.
38. Zplot for Windows, Electrochemistry, Impedance Software Operating Manual, Part 1, Scribner Ass. Inc., Southern Pines, NC **1998**.
39. J. E. Maslar, W. S. Hurst, W. J. Bowers Jr. and J. H. Hendricks*, J. Nucl. Mat.* **2001**, *298*, 239–247.
40. L. Kumari, G. H. Du, W. Z. Li, R. Selva Vennila, S. K. Saxena and D. Z. Wang, *Ceram. Int.* **2009***, 35*, 2401–2408.
41. F. Agulló-Rueda, in Ciencia e Ingeniería de la superficie de los materiales metálicos, A. J. Vazquez Vaamonde and J. J. de Damborenea Gonzalez Ed, Raycar S. A. Publishing, Madrid, **2000,** p. 570.
42. G. Gottardi, N. Laidani, V. Micheli, R. Bartali and M. Anderle*, Surf. Coat Technol*. **2008**, *202*, 2332–2337.
43. N. Sato, *Corros. Sci*. **1990**, 31, 1–19.
44. G. A. H. Mekhemer, *Colloids Surf. A*. **1998**,*141*, 227–235.
45. A. Gomez Sanchez, W. Schreiner, G. Duffó and S. Ceré, *Appl. Surf. Sci*. **2011**, *257* 6397–6405.
46. C. Combes, C. Rey and M. Freche, *Colloids Surface B*. **1998**, *11*, 15–27.
47. C. C. Chusuei, D. W. Goodman, M. J. Van Stipdonk, D. R. Justes, and E. A. Schweikert, *Anal. Chem*. **1999**, *71*, 149– 153.
48. C. Morant, J. M. Sanz, L. Galan, L. Soriano and F. Rueda, *Surface Sci*. **1989**, *218*, 331–345.
49. D. Wagner in Practical Surface Analysis, Vol. 1, D. Briggs and M. P. Seah, Ed. John Wiley & Sons Ltd, Chichester, **1996**, p. 611.
50. M. Matsuoka, S. Isotani, S. Miyake, Y. Setsuhara, K. Ogata and N., Kuratani, *J. Appl. Phys.* **1996**, *80*, 1177–1182.
51. Y. Nishino, A. R. Krauss, Y. Lin and D. M. Gruen*, J. Nuclear Mater*. **1996**, *228*, 346–353.
52. C. O. de Gonzalez and E. A. Garcia, *Surface Sci*. **1988**, 193, 305–320.
53. J. R. Macdonald, Impedance spectroscopy emphasizing solid materials and systems, John Wiley & Sons, New York. **1987**. p 12–16.
54. M. Orazem and B. Tribollet, Electrochemical Impedance spectroscopy (ECS), T. Wiley, New York 2008.p 159–16.
55. M. M. Khonsari and E. R. Booser, Applied Tribology. 2nd Ed., John Wiley & Sons Ltd, Chichester .**2008**.p 3–23
56. C. M. Mate, Tribology on the Small Scale - A Bottom Up Approach to Friction, Lubrication, and Wear, Oxford University Press, Oxford**. 2007**. p 24–35.

57. W. P. Dong, P. J. Sullivan and K. J. Stout, *Wear.* **1994***, 178*, 29–43.
58. C. Cox*, J. Electrochem. Soc*. **1970**, *117,* 654–663.
59. P. Meisterjahn, H. W. Hoppe and J. W. Shultze, *J. Electroanal. Chem*. **1987**, *217*, 159–185.
60. M. J. Madou and K. Kinoshita, *Electrochim. Acta.* **1984***, 29*, 411–417.
61. V. D. Jovic and B. M. Jovic*, Corros. Sci*. **2008***, 50*, 3063–3069.
62. (a) A. Goosens, M. Vazquez and D. D. Macdonald, *Electrochim. Acta.* **1996**, *41*, 35–45; (b) H. H. Kung, H. S Jarrett, A. W. Sleight and A. Ferretti, J Appl. Phys. **1977**, *48*, 2643–2649.
63. R. De Gryse, W. P. Gomes, F. Cardon and J. Vennik, *J. Electrochem. Soc*. **1975**, *122*, 711.
64. F. Cardon and W. P. Gomes, *J. Phys. D: Appl. Phys.* **1978**, *11*, L63.
65. W. J. Albery, G. J. O'Shea and A. L. Smith, *J. Chem. Soc., Faraday Trans*. **1996**, *92*, 4083–4085.
66. Y. Chen, M. Urquidi-Macdonald and D. D. Macdonald, *J. Nucl. Mater*. **2006**, 348, 133.
67. J. Ai, Y. Chen, M. Urquidi-Macdonald and D. D. Macdonald, *J. Electrochem. Soc*. **2007,** *154*, C43–51.
68. M. Bojinov, W. Cai, P. Kinnunen and P. Saario, *J. Nucl. Mater.* **2008***, 378*, 45–54.
69. J. Ai, Y. Chen, M. Urquidi-Macdonald and D. D. Macdonald, *J. Nucl. Mater*. **2008**, *379*, 162–168.
70. J. Sikora, E. Sikora and D. D. Macdonald*, Electrochim. Acta.* **2000**, *45*, 1875–1883.
71. S. K. Kima and C. S. Hwang, *Electrochem. Solid-State Lett.* **2008**, *11,* G9-G11.
72. X. Zhao and D. Vanderblitt, *Phys. Rev. B*. **2002**, *65*, 075105/1–075105/10.
73. A. M. Schmidt, D. S. Azambuja and E. M. A. Martini, *Corros. Sci*. **2006**, *48*, 2901–2912.
74. G. Vazquez and I. Gonzalez, *Electrochim. Acta.* **2007**, *52*, 6771–6777.
75. K. Azumi, T. Ohtsuka and N. Sato, *J. Electrochem. Soc*. **1987,** *134–136*, 1352–1357.
76. C.-O. A. Olsson and D. Landolt, *Electrochim. Acta*. **2003**, *48*, 3999–4011.
77. J. J. Noël, D. W. Shoesmith and Z. Tun, *J. Electrochem. Soc*. **2008**, *155*, C444–C454.
78. T. Pauporté and J. Finne, *J. Appl. Electrochem*. **2006,** *36*, 33–41.
79. O. E. Linarez Perez, V. C. Fuertes, M. A. Perez and M. Lopez Teijelo, *Electrochem. Comm*. **2008**, *10*, 433–437.
80. E. M. Patrito, R. M. Torresi, E. P. M Leiva and V. A. Macagno, *J. Electrochem. Soc*. **1990**, *137*, 524–530.
81. W. A. Badawy, S. S. Elegamy and Kh. M. Ismail, *Br. Corros. J*. **1993**, *28,* 133–136.
82. O. Kerrec, D. Devilliers, H. Groul and M. Chemla, *Electrochim. Acta*. **1995**, *40*, 719–724.
83. M. J. Esplandiu, E. M. Patrito and V. A. Macagno, *Electrochim. Acta*. **1995**, *40*, 809–815.
84. D. J. Blackwood, *Electrochim. Acta*. **2000**, *46,* 563.569.
85. F. Mansfeld and C.H. Tsai, *Corrosion.* **1991**, *47*, 958–972.
86. M. Aziz-Kerrzo, K. G. Conroy, A. M. Fenelon, S. T. Farrell and C. B. Breslin, *Biomaterials.* **2001**, *22*, 1531–1539
87. F. Mansfeld*. Electrochim. Acta.* **1990,** *35*,10. 1533–1544.
88. J. Pan, D. Thierry, C. Leygraf. *Electrochim. Acta.* **1996**, *41* (7/8), 1143–1153.
89. A. M. Fekry, Rabab M. El-Sherif. *Electrochim. Acta.* **2009,** *54,* 7280–7285.
90. M. E. P. Souza, L. Lima, C. R. P. Lima, C. A. C. Zavaglia and C. M. A. Freire. *J. Mater Sci: Mater Med.* **2009,** *20*, 549–552.
91. E. M. Patrito and V. A. Macagno*, J. Electroanal. Chem*. **1994,** *375*, 203–209.
92. J.-B. Jorcin, M. E. Orazem, N. P. Pébère and B. Tribollet, *Electrochim. Acta***.** **2006**, *51*, 1473–1478.
93. G. J. Brug, A. L. G. Van Den Eeden, M. Sluyters-Rehbach and J. H. Sluyters, *J. Electroanal. Chem*. **1984,** *176*, 275– 295.
94. C. H. Hsu and F. Mansfeld, *Corrosion.* **2001**, *57*, 747–748.
95. B. Hirschorn, M. Orazem, B. Tribollet, V. Vivier, I. Frateur and M. Musiani, *Electrochim. Acta.* **2010**, *55*, 6218–6223.
96. D. T. Chin, H. H. Chang. *J. of Appl. Electrochem.*. **1989,** *19,* 95–99.

Povzetek

Z namenom raziskati možnosti modifikacije površine za uporabo v biomedicinskih in elektronskih aplikacijah smo raziskali dielektrične lastnosti cirkonijevega oksida, ki se tvori z elektrokemijsko oksidacijo cirkonija v 1 M raztopini fosforjeve kisline med 3 V in 30 V. Oksidne plasti, ki smo jih pripravili pri različnih potencialih, smo analizirali z mikroskopom na atomsko silo, rentgensko fotoelektronsko spektroskopijo in Ramansko spektroskopijo. Slednji dve analizi sta pokazali, da se fosfatni ioni vgradijo v pasivno plast. Potencial ravnega pasu, ki smo ga določili na podlagi Mott-Schotky-jeve analize, nakazuje na dvojno strukturo plasti. Meritve elektrokemijske impedančne spektroskopije so bile osnova za izračun dielektrične konstante oksida. Na podlagi modela oksidne plasti smo ugotovili, da so vrednosti neodvisne of potenciala oksidacije